

Properties of the electron-doped layered manganates $\text{La}_{2-2x}\text{Ca}_{1+2x}\text{Mn}_2\text{O}_7$ ($0.6 \leq x \leq 1.0$)

Ian D. Fawcett, Eungsoo Kim, and Martha Greenblatt

Department of Chemistry, Rutgers, The State University of New Jersey, Piscataway, New Jersey, 08854

Mark Croft

Department of Physics and Astronomy, Rutgers, The State University of New Jersey, Piscataway, New Jersey 08854

Leonid A. Bendersky

Metallurgy Division NIST, 100 Bureau Drive, Stop 8554 Gaithersburg, Maryland 20899-8554

(Received 24 January 2000)

The $\text{La}_{2-2x}\text{Ca}_{1+2x}\text{Mn}_2\text{O}_7$ ($0.6 \leq x \leq 1.0$) series has been successfully synthesized using a citrate gel technique in order to study their structure and properties as a function of x in the Mn^{4+} -rich region of the phase diagram. Rietveld refinement of powder x-ray diffraction data, combined with electron microscopy, shows that the phases are of high purity and adopt the $n=2$ Ruddlesden-Popper structure comprised of perovskite bilayers separated by rocksalt layers. The lattice parameter c reaches a minimum at $x \sim 0.7$ and the increase with x is attributed to elongation of the apical Mn-O bonds due to preferential A-site occupancy and/or splitting of the t_{2g} levels of Mn^{4+} . X-ray absorption spectroscopy measurements confirm that the Mn-valence variation in these series tracks formal valence expectations. In the region $0.6 \leq x \leq 0.8$ the magnetic susceptibility manifests a peak or shoulder at ~ 280 K due to charge and orbital ordering, and antiferromagnetic order develops at lower temperatures ($T_N \sim 150$ – 200 K) with quasi-two-dimensional antiferromagnetic fluctuation effects being evidenced above T_N . The magnetic properties change significantly at $0.825 \leq x \leq 1.0$: at higher temperatures two-dimensional magnetic coupling is observed and at ~ 115 K the system spontaneously orders antiferromagnetically, but with a ferromagnetic moment. The transport results indicate insulating behavior at all compositions, but with an enhanced localization upon charge/orbital ordering in the $x=0.7$ material.

I. INTRODUCTION

Manganates, $L_{1-x}A_x\text{MnO}_3$ (where L and A represent trivalent rare-earth and divalent alkaline-earth ions, respectively), with perovskite structure have been the subject of intense research due to their fascinating magnetic and electrical properties, such as colossal magnetoresistance (CMR) Ref. 1 and charge ordering.² Explanations for these phenomena are generally concerned with the behavior of the manganese t_{2g} and e_g electrons. For example, double exchange³ involves ferromagnetic (FM) spin coupling between Mn^{3+} and Mn^{4+} with the conduction electrons mediating the interaction. Other instabilities, such as charge and orbital ordering and antiferromagnetic (AF) superexchange, compete with double exchange, leading to complex phase diagrams in which the properties of the manganate are extremely sensitive to many factors, such as the nature and relative concentration of the dopant atom.^{4,5}

The perovskite structure can be regarded as the $n=\infty$ end member of the Ruddlesden-Popper (RP) series $(\text{AO})(\text{ABO}_3)_n$.⁶ The structure of the RP series consists of perovskitelike blocks n octahedra thick, separated by a rock-saltlike AO layer. In the $n=2$ RP phase studied in this paper, two BO_6 corner-sharing slabs of octahedra alternate with AO rocksalt layers, shown in Fig. 1.

The structural consequences of moving from the perovskite ($n=\infty$) to a layered RP phase (where $n<\infty$) are the introduction of a two-dimensional (2D) character and a reduction from 6 to 5 in the number of nearest-neighbor manganese atoms around sites at the edge of the $(\text{ABO}_3)_n$ slabs.

It is well established that electron correlations are enhanced in two-dimensional (LD) materials. Hence, for these compounds with a lower dimensionality than that of the three-dimensional perovskite manganates, the magnetotransport phenomena are expected to be interesting in terms of anisotropic transport and exchange interactions.

Research into the properties of the $n=2$ RP manganate phases has mainly focussed on the $\text{La}_{2-2x}\text{Sr}_{1+2x}\text{Mn}_2\text{O}_7$ series.⁷ Of note, the $n=2$ RP manganates display a high magnetoresistance effect⁸ compared to the other members of the RP series, including the perovskite manganates. Investigations of the $(\text{Nd}, \text{Sr})n=2$ phases have revealed them to be biphasic, exhibiting CMR behavior, but without three-dimensional (3D) ferromagnetic long-range order.⁹

The properties of the $\text{La}_{2-2x}\text{Ca}_{1+2x}\text{Mn}_2\text{O}_7$ series have been examined in the Mn^{3+} -rich (hole-doped) region of the phase diagram. When $x=0.22$ – 0.50 , the compounds undergo an insulator-metal (IM) and paramagnetic-ferromagnetic transition.^{10,11} However, unlike in the 3D $n=\infty$ perovskites, the IM transition takes place at a lower temperature than the FM transition. This has been rationalized on the basis of two transition temperatures due to anisotropic exchange interactions. Upon lowering the temperature the higher transition is to a phase of 2D in-plane ordering, and the lower one leads to full 3D ordering and a metallic phase.¹⁰

Here we report on the preparation, structure, and properties of the $\text{La}_{2-2x}\text{Ca}_{1+2x}\text{Mn}_2\text{O}_7$ series in the electron-doped region $0.6 \leq x \leq 1.0$ of the phase diagram. The series has been successfully synthesized to higher values of x in order to

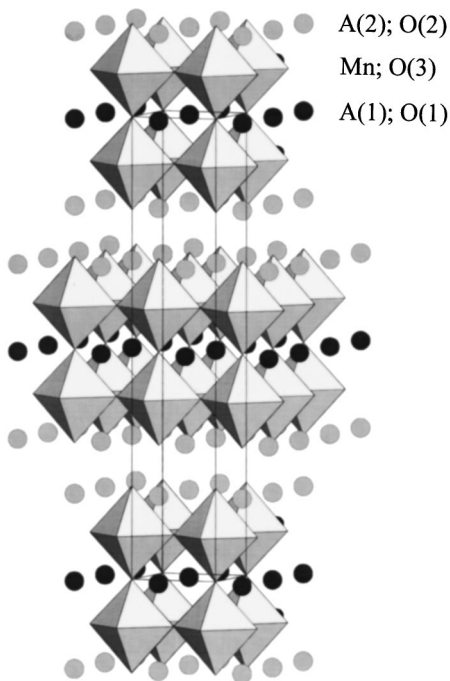


FIG. 1. The $n=2$ Ruddlesden-Popper structure of $\text{La}_{2-2x}\text{Ca}_{1+2x}\text{Mn}_2\text{O}_7$.

investigate the fascinating electronic and magnetic properties. This is compared and contrasted with the perovskite manganates over the same doping region.

II. EXPERIMENT

Samples of $\text{La}_{2-2x}\text{Ca}_{1+2x}\text{Mn}_2\text{O}_7$ were prepared from La_2O_3 (Alfa Aesar, 99.99%, dried in air at 800°C prior to use), CaCO_3 (Aldrich, 99+%), and $\text{Mn}(\text{NO}_3)_2$ (Aldrich, 49.7 wt % solution in dilute nitric acid). Stoichiometric amounts of the starting materials were dissolved in approximately 25 cm^3 4 M HNO_3 to which was added an excess of citric acid (Aldrich, 99.5%) and ethylene glycol (Aldrich, 99+%) with respect to metal-complex formation. After all the reactants had dissolved, the solution was heated on a hot plate resulting in the formation of a gel. The gel was dried at 300°C , then heated to 600°C to remove the organic matter and to decompose the nitrates. The resultant ash was pressed into pellets, and fired at 1250°C for 24 h, then quenched to room temperature. After regrinding and pressing into pellets, this process was repeated.

The oxidation state of manganese in the products was determined with iodometric titrations as described by Licci *et al.*¹²

Powder x-ray diffraction (PXD) data were measured with a Scintag Pad-V diffractometer employing $\text{CuK}\alpha$ radiation over the range $5^\circ \leq 2\theta \leq 120^\circ$, with a step size of 0.02° . Rietveld refinement of the data was undertaken using the GSAS Rietveld refinement program.¹³ A broad maximum seen in the background of the x-ray diffraction patterns was due to the glass slide used to hold the samples. Although refinement of laboratory powder x-ray diffraction data does not generally give reliable oxygen positions, we have used the results to report overall trends in the data.

Temperature-dependent susceptibility measurements were

made with a Quantum Design superconducting quantum interference device (SQUID) magnetometer over the temperature range 5–400 K in an applied field of 1000 G. Data were collected after cooling in zero field [zero-field cooling (ZFC)] and in an applied field (FC).

Resistivity measurements were made using a standard four-probe method. Gold wire contacts were attached to the sintered polycrystalline samples with silver paint.

The Mn K -edge x-ray absorption spectroscopy (XAS) measurements were performed on beam lines X-19A and X-18B at the Brookhaven National Laboratory synchrotron light source using double crystal and channel-cut Si(111) monochromators, respectively. Electron yield, fluorescence mode, and transmission mode measurements were made and checked for consistency. A standard was run simultaneously with all the measurements for precise calibration. The relative energies between various spectra were established by careful comparison of the standard spectra. In general, the relative accuracy of the energy is about ± 0.05 eV. All spectra were normalized to unity step in the absorption coefficient from well below to well above the edge.

Specimens with $x=0.6$ and 0.9 were examined by transmission electron microscopy (TEM). The $x=0.6$ specimens were prepared by dispersing powder that had been crushed in acetone onto lacey-carbon coated copper grids. The $x=0.9$ specimens were prepared from pellets by conventional polishing, dimpling, and ion thinning. The specimens were examined using a Phillips 430 TEM microscope operated at 200 kV.

III. RESULTS AND DISCUSSION

A. Synthesis

Synthesis of the $n=2$ manganates is notoriously difficult, and biphasic samples can be formed¹⁴ that appear to be monophasic by analysis of laboratory powder x-ray diffraction data alone. The preparation is sensitive to many factors including temperature, heating time, and the cooling process¹⁵ more so than for the perovskite manganates. For example, the phase diagram for $\text{La}_{2-2x}\text{Sr}_{1+2x}\text{Mn}_2\text{O}_7$ has recently been extended into the Mn^{4+} -rich region via a two-step process: high-temperature firing (1650°C) followed by quenching into dry ice, then low-temperature annealing (400°C) to fill oxygen vacancies.¹⁶

The preparation of the $\text{La}_{2-2x}\text{Ca}_{1+2x}\text{Mn}_2\text{O}_7$ series was attempted using a variety of conditions. The citrate gel technique was used because it has the advantages of smaller particle size and greater sample homogeneity over standard solid-state techniques. Firing the reaction mixture at lower temperatures (1000 – 1200°C) produced a mixture of the $n=2$ RP phase, the perovskite, and unreacted CaO/CaCO_3 . At higher reaction temperatures ($\geq 1300^\circ\text{C}$), the majority $n=2$ RP phase was contaminated by small perovskite impurities. There was also a loss in crystallinity as evidenced by broad peaks in the PXD pattern attributed to the creation of oxygen vacancies. We found that a temperature of 1250°C and quenching to room temperature were optimal conditions for the preparation of the phases studied in this paper.

Samples with $x \leq 0.5$ could not be prepared without the presence of perovskite impurities, which became the majority phase at lower values of x . A detailed analysis of crystal-

lites with $x \leq 0.5$ by electron microscopy revealed large intergrowths of $n=2$ and $n=\infty$ phases. Measurements of the magnetic and electrical properties of such $x \leq 0.5$ materials showed a variation with x , similar to that observed in previous work,¹⁰ i.e., an insulator-metal transition occurring at a significantly lower temperature than the ferromagnetic transition.

The oxygen content, determined by iodometric titration, indicated that the samples were slightly oxygen deficient due to quenching the reaction to room temperature from high temperatures (1250 °C). Further studies of the Mn oxidation state were determined with x-ray absorption spectroscopy, as described below.

B. Structure: X-ray diffraction

Preliminary characterization of the samples was undertaken with powder x-ray diffraction. In order to identify whether an $n=2$ RP phase had formed, data were collected over the range $5^\circ \leq 2\theta \leq 120^\circ$. The data below 15° , which should contain no reflections due to simple perovskite impurities, were analyzed for the 002 reflection (at $\sim 9^\circ$), characteristic of the $\text{La}_{2-2x}\text{Ca}_{1+2x}\text{Mn}_2\text{O}_7$ series. Further analyses of the PXD data, which contain the 002 reflection, were undertaken with Rietveld refinements.

Refinements were carried out in the tetragonal space group $I4/mmm$. The background was modeled by Chebyshev polynomials of the first kind and the peak shape was described by a pseudo-Voigt function. The isotropic thermal parameters for La/Ca(1) and La/Ca(2) were constrained to refine together and likewise for O(1), O(2), and O(3). There are two sites in the $n=2$ RP structure over which the La and Ca can be distributed: a 12-coordinate site [La/Ca(1)] in the perovskitelike blocks and a 9-coordinate site [La/Ca(2)] in the rocksalt units. Using as constraints the total amount of La and Ca in the sample and assuming unit occupancy at each site, the distribution of La and Ca was allowed to refine over the two sites. The x-ray diffraction patterns, including the raw data, the fitted profile, and the difference profile for three representative members of the series with $x=0.6$, 0.8, and 1.0, are shown in Fig. 2. The RP phases were assumed to be monophasic at the resolution of a laboratory x-ray diffractometer. However, a careful examination of the profiles during the refinement revealed small, unidentified impurity peaks not associated with the title phases or a perovskite impurity.

The variation of the lattice parameters a and c with x is plotted in Fig. 3. As x increases, we note that the a parameter decreases nonlinearly with a noted downturn at $x \sim 0.8$, which coincides with a change in the magnetic susceptibility curves, discussed below, and the c parameter reaches a minimum at $x \sim 0.7$. This behavior is contrary to that observed in the hole-doped region in which the lattice parameters decrease as x increases.¹⁰ When $x > 0.5$, Asano *et al.*¹⁰ and Millburn *et al.*¹⁶ (in the $\text{La}_{2-2x}\text{Sr}_{1+2x}\text{Mn}_2\text{O}_7$ RP phases) also observe an increase in the c parameter.

The nonlinear nature of the plots of the lattice parameter as a function of x suggests the presence of either a structural transition or phase separation. However, all of the patterns could be indexed in the $I4/mmm$ space group. Analysis by electron microscopy, which is discussed below, also indi-

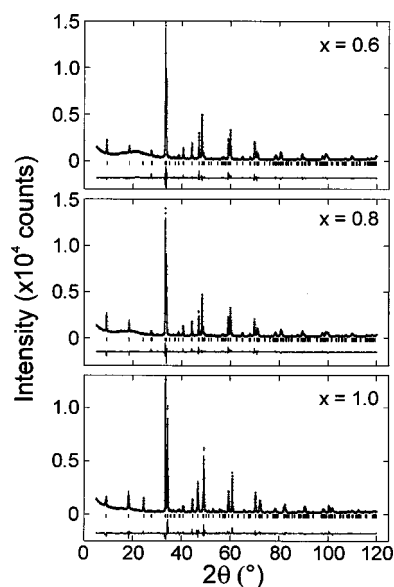


FIG. 2. Typical x-ray diffraction profiles for $\text{La}_{2-2x}\text{Ca}_{1+2x}\text{Mn}_2\text{O}_7$ (top to bottom): $\text{La}_{0.8}\text{Ca}_{2.2}\text{Mn}_2\text{O}_7$, $\text{La}_{0.4}\text{Ca}_{2.6}\text{Mn}_2\text{O}_7$ and $\text{Ca}_3\text{Mn}_2\text{O}_7$. Key: observed data (+) and calculated profile (solid line); difference plots drawn below each profile, and tick marks represent allowed reflections.

cated that the phases were of high purity and crystallized with the space group $I4/mmm$. In a related $n=2$ RP phase $\text{Sr}_3\text{Fe}_2\text{O}_{7-x}$,¹⁷ curves in the lattice parameter vs x plots were attributed to oxygen vacancies. However, iodometric titrations indicate that the title phases are only slightly oxygen deficient. The behavior of the curves, as noted by Millburn *et al.*¹⁶ for the $\text{La}_{2-2x}\text{Sr}_{1+2x}\text{Mn}_2\text{O}_7$ series, may reflect changes in the nature of orbital occupation and/or A -type ordering as a function of x , noted below.

In the structural refinements, we observe that the smaller Ca^{2+} ion preferentially occupies the nine-coordinate site [La/Ca(2)] in the rocksalt layer (Table I). This is most noticeable with lower values of x , where the higher fraction of La contributes significantly to the x-ray pattern. Studies of the $n=2$ RP manganates $L_{1.2}\text{Sr}_{1.8}\text{Mn}_2\text{O}_7$ ($L=\text{La}, \text{Pr}, \text{Nd}$) (Ref. 18) also show that the smaller A cation has greater preference for the smaller nine-coordinate site. The distribution of the A

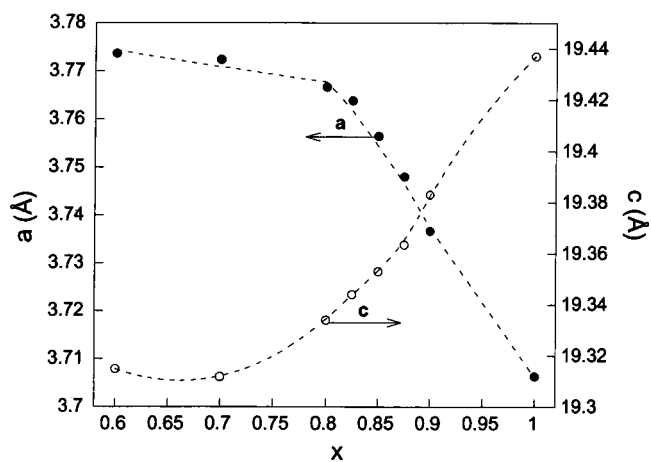


FIG. 3. The variation of the lattice parameters a and c with x for $\text{La}_{2-2x}\text{Ca}_{1+2x}\text{Mn}_2\text{O}_7$. (The dashed line acts as a guide to the eye.)

TABLE I. Structural parameters for $\text{La}_{2-2x}\text{Ca}_{1+2x}\text{Mn}_2\text{O}_{7-\delta}$.

Ideal formula	$\text{La}_{0.8}\text{Ca}_{2.2}\text{Mn}_2\text{O}_7$	$\text{La}_{0.6}\text{Ca}_{2.4}\text{Mn}_2\text{O}_7$	$\text{La}_{0.4}\text{Ca}_{2.6}\text{Mn}_2\text{O}_7$	$\text{La}_{0.35}\text{Ca}_{2.65}\text{Mn}_2\text{O}_7$	$\text{La}_{0.3}\text{Ca}_{2.7}\text{Mn}_2\text{O}_7$	$\text{La}_{0.25}\text{Ca}_{2.75}\text{Mn}_2\text{O}_7$	$\text{La}_{0.2}\text{Ca}_{2.8}\text{Mn}_2\text{O}_7$	$\text{Ca}_3\text{Mn}_2\text{O}_7$
x	0.6	0.7	0.8	0.825	0.85	0.875	0.9	1.0
	0	0.05	0.03	0.02	0.02	0.03	0.02	0.03
Formal oxidation state of Mn	3.6	3.65	3.77	3.81	3.83	3.85	3.88	3.97
$a/\text{\AA}$	3.7737(8)	3.7724(1)	3.7667(3)	3.7639(1)	3.7565(1)	3.7480(1)	3.7367(3)	3.7064(3)
$c/\text{\AA}$	19.3148(7)	19.3118(8)	19.335(1)	19.344(1)	19.3530(7)	19.3634(6)	19.383(2)	19.437(2)
$V/\text{\AA}^3$	274.97(1)	274.83(2)	274.32(6)	274.05(2)	273.09(2)	272.01(1)	270.63(6)	267.02(6)
c/a	5.118	5.119	5.133				5.187	5.244
La/Ca(1) <i>occ</i>	0.338(6)/0.662(6)	0.428(5)/0.572(5)	0.260(5)/0.740(5)	0.108(5)/0.892(5)	0.115(4)/0.885(4)	0.107(4)/0.893(4)	0.050(4)/0.950(4)	
La/Ca(2) z	0.3136(1)	0.3139(1)	0.3132(1)	0.3127(2)	0.3129(1)	0.3127(1)	0.3120(1)	0.3112(1)
La/Ca(2) <i>occ</i>	0.231(3)/0.0769(3)	0.086(2)/0.914(2)	0.070(2)/0.930(2)	0.121(2)/0.879(2)	0.093(2)/0.907(2)	0.071(2)/0.929(2)	0.075(2)/0.925(2)	
La/Ca $U_{\text{iso}}/\text{\AA}^2$	0.0130(9)	0.0059(8)	0.003(8)	-0.0008(8)	-0.0016(7)	-0.00156(6)	-0.0073(7)	0.0047(8)
Mn z	0.0986(2)	0.1006(2)	0.1006(2)	0.0971(2)	0.0973(2)	0.0978(2)	0.0976(2)	0.0995(1)
Mn $U_{\text{iso}}/\text{\AA}^2$	-0.0111(9)	-0.00179(8)	0.004(9)	0.007(1)	0.005(1)	0.0027(8)	-0.0021(9)	0.0078(8)
O(2) z	0.2015(6)	0.2008(6)	0.2040(7)	0.2090(7)	0.2078(6)	0.2048(6)	0.2064(6)	0.2020(5)
O(3) z	0.0974(5)	0.0956(5)	0.1030(4)	0.0943(5)	0.0945(5)	0.0953(5)	0.0955(4)	0.0986(4)
O $U_{\text{iso}}/\text{\AA}^2$	0.005(1)	0.011(1)	0.020(1)	0.027(2)	0.017(2)	0.014(1)	0.019(1)	0.030(1)
R_{wp}	0.0919	0.0911	0.1070	0.1050	0.1119	0.0997	0.0834	0.1117
R_p	0.0668	0.0702	0.0749	0.0776	0.0838	0.0712	0.0631	0.0840
χ^2_{red}	8.941 for 34 variables	5.775 for 34 variables	11.303 for 33 variables	10.370 for 31 variables	11.91 for 31 variables	10.41 for 30 variables	6.406 for 36 variables	11.23 for 35 variables
La/Ca(1)-O(1) $\times 4$	2.66796(6)	2.66750(7)	2.6634(1)	2.6615(1)	2.5621(6)	2.6502(1)	2.6422(2)	2.6208(2)
-O(3) $\times 8$	2.665(7)	2.639(7)	2.730(8)	2.621(7)	2.622(6)	2.630(6)	2.630(6)	2.666(5)
La/Ca(2)-O(2) $\times 1$	2.164(12)	2.185(12)	2.111(13)	2.008(14)	2.035(12)	2.089(11)	2.048(12)	2.121(11)
-O(2) $\times 4$	2.684(1)	2.683(1)	2.684(1)	2.694(2)	2.686(2)	2.672(2)	2.666(2)	2.633(1)
-O(3) $\times 4$	2.552(7)	2.571(7)	2.495(8)	2.603(8)	2.596(7)	2.586(6)	2.589(6)	2.552(5)
Mn-O(1) $\times 1$	1.904(4)	1.943(3)	1.946(4)	1.878(4)	1.883(4)	1.894(4)	1.891(4)	1.934(3)
-O(2) $\times 1$	1.989(12)	1.935(11)	1.998(13)	2.164(15)	2.138(13)	2.071(12)	2.109(12)	1.994(10)
-O(3) $\times 4$	1.8867(1)	1.8887(6)	1.8837(2)	1.8828(3)	1.8790(3)	1.8746(2)	1.8688(2)	1.8533(2)
Mn-O(3)-Mn	178.7(6)	174.1(6)	178.2(3)	176.7(7)	176.8(6)	177.1(5)	177.5(5)	179.0(5)
MnO_6 distortion ^a	1.6	1.3	2.3	3.5	3.4	2.8	3.4	2.9

^a $(r_{\text{ax}} - r_{\text{eq}}) \times 100\% / (r_{\text{ax}} + r_{\text{eq}})$

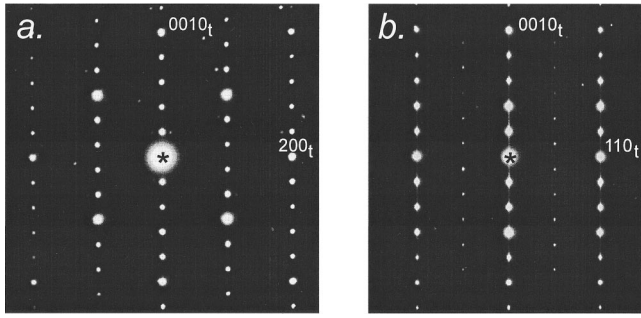


FIG. 4. Selected area diffraction (SAD) patterns taken from (a) $x=0.6$ and (b) $x=0.9$ specimens. Both patterns are indexed as $I4/mmm$ ($n=2$) structure, with (a) $[010]_t$ and (b) $[1-10]_t$ zone axes. In (b) a row of $1/2\ 1/2\ l$ weak extra reflections are evident.

cation is likely to affect the Mn-O bond lengths, particularly those along the c axis. In the MnO_6 octahedra, there are two apical Mn-O bonds, one directed to the center of the double perovskite slab $[\text{Mn-O}(1)]$ and the other points into the rock-salt layer $[\text{Mn-O}(2)]$, Fig. 1. While the variation of the Mn-O bond distances, as a function of x , in Table I, is not so systematic, the trend is clear. As x increases, the Mn-O(1) bond length remains fairly constant ($\Delta a_{\text{avg}} \sim 0.04 \text{ \AA}$) with x in the range $0.6 \leq x \leq 0.825$ and dramatically decreases from $x \geq 0.825$ with increasing x up to $x=0.9$. In contrast, we note a general increase in the Mn-O(2) bond length with increasing x and a significant increase ($\Delta c_{\text{avg}} \sim 0.1 \text{ \AA}$) in the $0.6 \leq x \leq 0.825$ range. One reason for this trend is that the smaller ion (Ca^{2+}) on the nine-coordinate site is surrounded by a smaller volume polyhedra than the ion (La^{3+}) occupying the larger 12-coordinate site, which draws the surrounding oxygen ligands towards it, hence elongating the Mn-O(2) bond which points to the rock-salt layer. Conversely, the elongation of the Mn-O(2) bond decreases the volume of the nine-coordinate polyhedron surrounding the A cation, thereby forcing the smaller ion to occupy this site. With an increase in x , the Mn-O(2) bond increases, and the c parameter increases.

We also observed distorted MnO_6 octahedra in the RP calcium manganates containing Mn exclusively in the 4+ oxidation state (i.e., $x=1$).¹⁹ We ascribed the elongation to a splitting of the t_{2g} orbitals, with the d_{xz} and d_{yz} orbitals being stabilized relative to the d_{xy} orbital (similar to the splitting found in a tetragonal transition-metal complex) which leads to a lowering of the electronic energy for the Mn^{4+} (d^3) configuration. In the RP manganates reported in this paper, the MnO_6 distortion increases as the amount of Mn^{4+} increases, which could be attributed to d -orbital splitting (Table I).

More detailed explanations of the properties require the relative occupancy of the 9- and 12-coordinate sites and the oxygen positions to be resolved to a higher degree of accuracy by the use of higher-resolution diffraction data. Neutron diffraction studies are currently being undertaken at a different laboratory with samples supplied by us.

C. Structure: Electron microscopy

Figure 4 shows examples of selected area diffraction (SAD) patterns typical for all specimens. Both patterns in

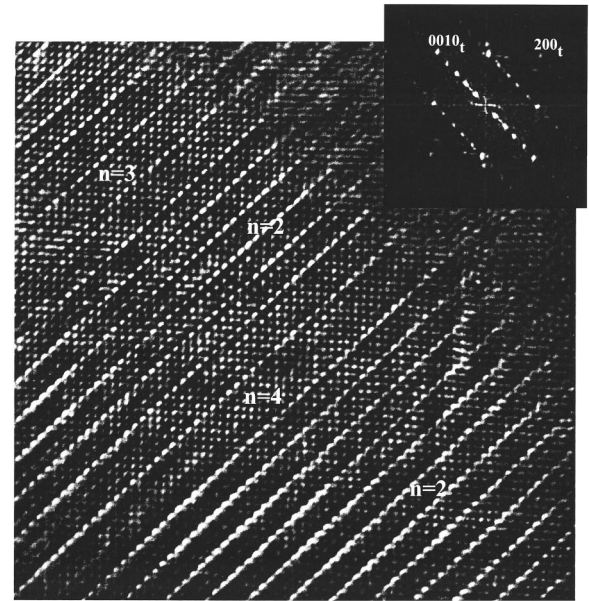


FIG. 5. High-resolution TEM image showing the presence of intergrowth in the predominately the $n=2$ structure. Blocks of $n=3$ and a layer of $n=4$ structure are indicated. The inset shows digital diffraction (fast Fourier transform) of the image.

Fig. 4 are indexed as the $I4/mmm$ ($n=2$) structure, with (a) $[010]_t$ and (b) $[1-10]_t$ zone axes, respectively. Typically, the SAD patterns exhibit a streaking of intensity along the $[001]_t$ direction, e.g., in Fig. 4(b). The streaking reflects the presence of planar defects normal to $[001]_t$. With the help of high-resolution imaging, the defects were shown to be intergrowth of individual layers or blocks with different number n of octahedra. Such an intergrowth region is shown in Fig. 5 where predominately the $n=2$ structure has blocks of $n=3$ and a layer of $n=4$ structure. The amount of intergrowth apparently diminishes with increasing Ca content.

In addition to the reflections of the $I4/mmm$ structure ($a_t=3.74 \text{ \AA}$, $c_t=19.36 \text{ \AA}$ for $x=0.9$), a row of $1/2\ 1/2\ l$

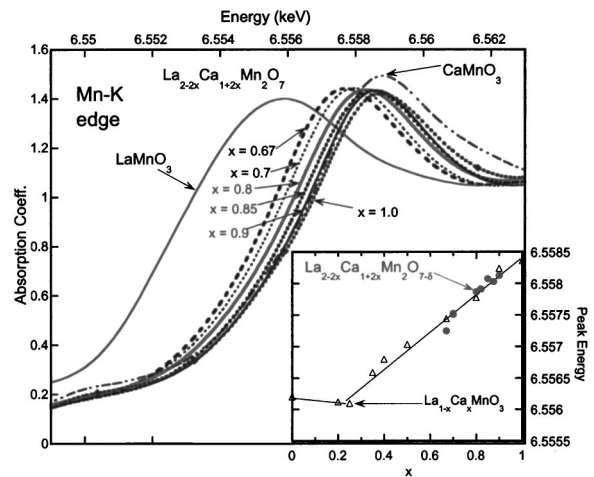


FIG. 6. The Mn K main edges of $\text{La}_{2-2x}\text{Ca}_{1+2x}\text{Mn}_2\text{O}_7$ ($x=0.6-1.0$) along with those of the CaMnO_3 and LaMnO_3 standards. Inset: the energy (chemical shift) of the peak of the Mn K main edges of $\text{La}_{2-2x}\text{Ca}_{1+2x}\text{Mn}_2\text{O}_7$ ($x=0.6-1.0$) along with those of the $\text{La}_{1-x}\text{Ca}_x\text{MnO}_3$ system (Ref. 21).

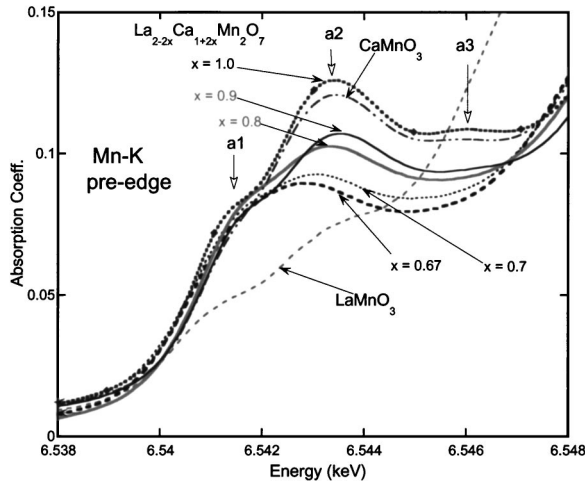


FIG. 7. The Mn *K* pre-edge features of $\text{La}_{2-2x}\text{Ca}_{1+2x}\text{Mn}_2\text{O}_7$ ($x=0.6-1.0$) compounds along with those of the CaMnO_3 and LaMnO_3 standards.

weak reflections is detected in the $[1-10]_t$ SAD pattern of $x=0.9$ specimen, Fig. 4(b). These reflections suggests a larger *a* parameter, $a' = \sqrt{2}a_t = 5.3 \text{ \AA}$. Observation of the extra reflections were also supported by convergent beam diffraction from grains at $[001]_t$ orientation. The work is in progress to establish the origin of the ordering, with a working hypothesis that the octahedra in a perovskite layer are tilted, probably due to the tolerance factor requirement.

D. Mn *K* XAS

The Mn *K* main edges for $\text{La}_{2-2x}\text{Ca}_{1+2x}\text{Mn}_2\text{O}_7$ ($x=0.67-1.0$) are shown in Fig. 6. There appears to be an extremely regular chemical shift of the spectra, with decreasing *x*, to lower energy. This is consistent with the trend seen in the perovskite $\text{La}_{1-x}\text{Ca}_x\text{MnO}_3$ system, with decreasing *x*/Mn valence.²⁰ Indeed, in Fig. 6, inset, the concentration *x*, dependences of the chemical shifts of the perovskite, and the 327 systems are seen to exhibit excellent agreement in the $x=0.67-1.0$ range. It is worth noting that the $x=0.6$ compound exhibits a departure from this correlation. The $x=0.6$ spectrum (not shown in Fig. 6) in fact falls close to that of the $x=0.7$. The $x=0.5$ material in this 327 series has been reported to exhibit ferromagnetic-metallic behavior.²¹ The proximity of the $x=0.6$ material to this phase change could be related to this deviation in the XAS chemical shift: however, further work on this issue is needed.

The Mn *K* pre-edge features, related to transitions into final *d* states, for the $\text{La}_{2-2x}\text{Ca}_{1+2x}\text{Mn}_2\text{O}_7$ ($x=0.67-1.0$) compounds are shown in Fig. 7. The $x=1.0$ ($\text{Ca}_3\text{Mn}_2\text{O}_7$) pre-edge spectrum manifests the *a*1-shoulder feature, the

main *a*2-peak feature, and the subtle *a*3-peak feature first identified in the CaMnO_3 perovskite pre-edge.²² Despite having the same formal Mn valence, comparison of $\text{CaMnO}_{3-\delta}$ perovskite and the $x=1.0$, $\text{La}_{2-2x}\text{Ca}_{1+2x}\text{Mn}_2\text{O}_7$ pre-edges reveals that the 327 pre-edge has on overall greater spectral intensity, a much more pronounced *a*1 feature, and a more discernible *a*3-feature.

In this 327 compound the *c*-axis/apical-Mn-O bond lengths on the interior [$\text{Mn-O}(1) \sim 1.9 \text{ \AA}$] and the border [$\text{Mn-O}(2) \sim 2.0 \text{ \AA}$] of the MnO_6 bilayers do not have symmetrical bond lengths. In fact, the Mn-O(2) distance appears to be particularly elongated. This could modify both the overall intensity and energy distribution of the pre-edge features. The lack of centrosymmetry allows enhanced mixing of dipole allowed *p* states into the pre-edge feature final states. This effect would be consistent with the overall pre-edge intensity enhancement in the $x=1.0$, 327 spectrum. Both simple electronic structure arguments and local density approximation (LDA)+*U* calculations²³ for the perovskite compounds indicate that the lowest unfilled *d* states (those contributing to the *a*1 feature) are the majority-spin e_g states. The Mn-O(2) bond elongation towards the rocksalt layer and the asymmetry of the apical Mn-O bonds imply loss of bonding and increased localization of the Mn e_g states. The increased prominence of the *a*1 feature would be consistent with modification of these states and the potential for their more localized character.

In the $\text{La}_{1-x}\text{Ca}_x\text{MnO}_3$ system the decrease in Mn valence, associated with decreasing *x*, has been shown to correlate with the decrease in the intensity of the Mn *K* pre-edge features and with the decrease of the intensity of the *a*2 feature, relative to the *a*1 feature.²⁰ The LaMnO_3 and CaMnO_3 perovskite spectra in Fig. 7 illustrate clearly the end points of these intensity changes. The pre-edges for the $\text{La}_{2-2x}\text{Ca}_{1+2x}\text{Mn}_2\text{O}_7$ ($x=0.67-1.0$) series, shown in Fig. 7, both show such an *a*2-feature degradation and overall intensity decrease with decreasing *x*. Thus the pre-edge variation further support the Mn-valence decrease with decreasing *x* for $x=1.0-0.67$ in this system. Again (as in the case of the chemical shift), it should be noted that the $x=0.6$ pre-edge spectrum deviated from this trend, resembling the $x=0.7$ spectrum.

E. Magnetic and resistivity results

Our temperature-dependent susceptibility [$\chi(T)$], and resistivity [$\rho(T)$] results are shown in Figs. 8(a)–8(h) and Table II. The insets of these figures show the high-temperature inverse susceptibility [$\chi^{-1}(T)$] behavior with the region of Curie Weiss (CW) behavior indicated by a line. The magnetic behavior in these materials is somewhat com-

TABLE II. Magnetic properties of $\text{La}_{2-2x}\text{Ca}_{1+2x}\text{Mn}_2\text{O}_{7-\delta}$.

<i>x</i>	0.6	0.7	0.8	0.825	0.85	0.875	0.9	1.0
θ/K (350–400 K)	−67	−37	−92	−33	−93	−95	−125	−465
T_{CO}/K	280	275	275					
T_{N}/K	140	110	117					165
T_{F}/K				110	110	115	115	115

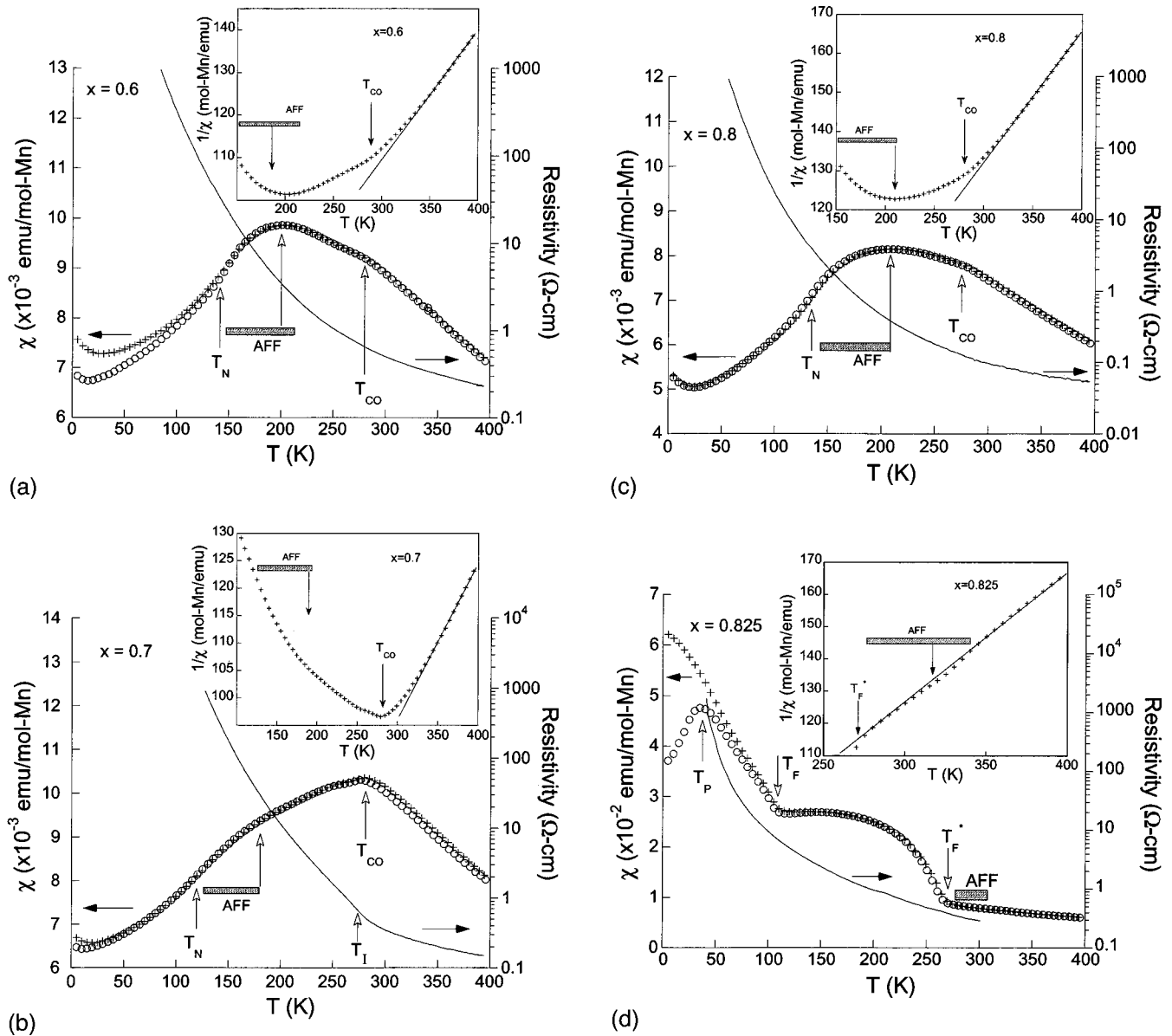


FIG. 8. (a)–(h) The temperature dependence of the magnetic susceptibility (χ) and resistivity for $\text{La}_{2-2x}\text{Ca}_{1+2x}\text{Mn}_2\text{O}_7$. Inset: inverse susceptibility vs temperature. The crosses and circles represent χ data collected under field-cooled (FC) and zero-field-cooled (ZFC) conditions, respectively. Note that characteristic temperatures associated with specific features in these curves have been identified: T_N and T_{CO} are associated with AF and charge- and orbital (CO) ordering temperatures, respectively; T_l is the temperature of the logarithmic inflection point of the resistivity curve for $x=0.7$; the solid line in the insets represent the regions modeled with the CW form, $\chi^{-1} = (T - \theta)/C$; T_F denotes the temperature of the onset of a FM moment at the canted-AF (CAF) ordering in the $0.85 \leq x \leq 1.0$ range; the temperature range above the long-range magnetic ordering temperature (T_N) where evidence has been found for short-range antiferromagnetic fluctuations (AFF's) is indicated by dotted-shading. T_F^* is analogous with T_F for the $x=0.825$ sample, but is differentiated due to its anomalously high temperature; finally note the temperatures T_P , which identify the ZFC, low-temperature maxima in the susceptibility in the $x > 0.8$ range.

plex. Consequently, features in the results in Figs. 8(a)–8(h), which are subsequently used to infer the phase diagram (Fig. 9) of the system, have been identified for clarity.

We will consider first the high-temperature dependence of the magnetic susceptibility, shown in Figs. 8(a)–8(h) along with the inverse susceptibility (on an expanded scale) in the insets. At the highest temperatures the susceptibility increases with decreasing temperature with the inverse susceptibility approaching linear CW-like behavior [$\chi = C/(T - \theta)$] in a range indicated by the solid lines in the figure insets. Fitting these data in these T ranges yielded Weiss

constants θ , which are plotted in Fig. 9, top. Although Fig. 9, middle, and 9, bottom, will be discussed at length in a subsequent section, they will be introduced here for clarity. In Fig. 9, middle, the low-temperature (10 K) χ and room-temperature resistivity (ρ_{RT}) are plotted. In Fig. 9, bottom, the temperature-concentration (x) phase diagram, as inferred from the magnetic and transport data, is summarized.

In Fig. 9, top, the dashed horizontal line represents the approximate long-range AF ordering temperature (T_N), inferred below, for most of the materials in this series. It is important to note that although the Weiss constants are con-

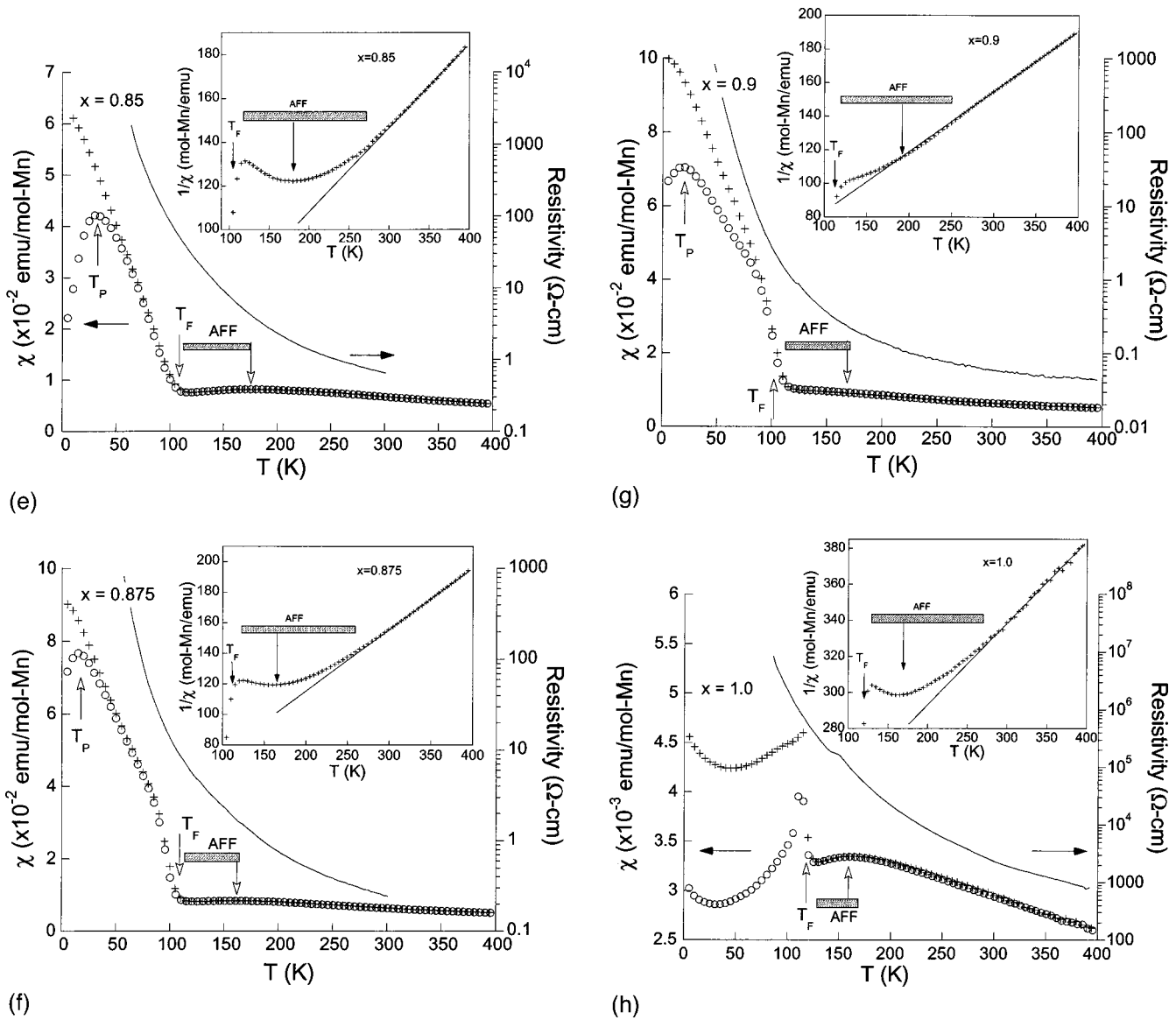


FIG. 8. (Continued).

sistent with AF interactions, the θ values fall substantially below the ordering temperature for $x < 0.9$. Moreover, at $x = 1.0$ the θ value is roughly fourfold too high to agree with the AF ordering temperature. Fawcett *et al.*¹⁹ have previously discussed the disproportionately large θ values (and their decrease with n) in the RP phases $\text{Ca}_{n+1}\text{Mn}_n\text{O}_{3n+1}$ in terms of covalency reduction in the Mn moments. Hence both substantial covalency and AF interactions would be expected to produce quite large negative θ values in the $\text{La}_{2-2x}\text{Ca}_{1+2x}\text{Mn}_2\text{O}_7$ materials studied here. We therefore argue that the low θ values in the $x < 0.9$ regime in fact are probably related to FM correlations in the high-temperature range, namely, a positive FM contribution to a larger negative (covalency-related) θ value.

Indeed FM double-exchange coupling due to the presence of hopping between Mn^{3+} and Mn^{4+} is expected at high temperatures in these materials. In perovskite manganates over a similar x range, e.g., $\text{Bi}_{1-x}\text{Ca}_x\text{MnO}_3$ ($0.41 \leq x \leq 0.82$),^{24,25} ferromagnetic spin correlations are observed at high temperatures. The variations in the observed θ values (for $x < 0.9$) in Fig. 9, top, are presumably related to varia-

tions in the strength of the FM correlations. The rapid rise in θ for $x > 0.9$ reflects the dominance of the covalency effects, as the FM correlations are destroyed by the suppression of the $\text{Mn}^{3+}/\text{Mn}^{4+}$ FM double exchange as is analogously seen in the $\text{Bi}_{1-x}\text{Ca}_x\text{MnO}_3$ and $\text{La}_{1-x}\text{Ca}_x\text{MnO}_3$ perovskite systems.^{24,25} Within this interpretation the high-temperature range of the phase diagram, in Fig. 9, bottom, is labeled by FMF for ferromagnetic fluctuations in the $x \leq 0.9$ range.

At a temperature of approximately 280 K, denoted by T_{CO} , the susceptibility reaches a maximum for the $x = 0.7$ material [see Fig. 8(b)]. The resistivity at this composition also shows a nonlinear increase [with a well-defined negative peak in $d(\ln \rho)/dT$] at $T_1 = 280$ K coinciding with T_{CO} . Thus this $x = 0.7$ material manifests thermal magnetic and resistivity behavior essentially identical to those observed at the charge- and orbital- (CO) ordering temperatures of $\text{La}_{1-x}\text{Ca}_x\text{MnO}_3$ materials:^{26,27} namely, coincident peaks in $-d(\ln \rho)/dT$ and $\chi(T)$. Also the high-temperature θ parameter is particularly low (see Fig. 9, top) at $x = 0.7$, indicating (within the argument above) that the high-temperature FM

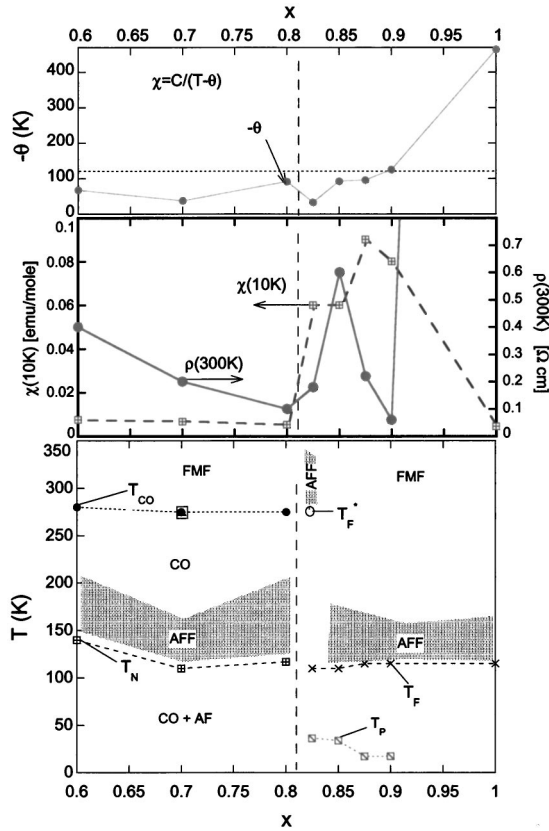


FIG. 9. **Top:** the high-temperature paramagnetic θ values vs x for the $\text{La}_{2-2x}\text{Ca}_{1+2x}\text{Mn}_2\text{O}_7$ system. Note that the small θ values compared to the AF-ordering temperature (T_N) scale (dotted line) is taken as an indicator of ferromagnetic fluctuations (FMF's) at high temperatures. **Middle:** The room-temperature (300 K) resistivity values $\rho(300\text{ K})$ and low-temperature susceptibility values $\chi(10\text{ K})$ vs x for the $\text{La}_{2-2x}\text{Ca}_{1+2x}\text{Mn}_2\text{O}_7$ system. **Bottom:** The phase diagram for the $\text{La}_{2-2x}\text{Ca}_{1+2x}\text{Mn}_2\text{O}_7$ system. At high temperatures ferromagnetic fluctuations (FMF's) due to $\text{Mn}^{3+}/\text{Mn}^{4+}$ hopping are assumed to be present. The temperatures labeled T_{CO} are the locus of the higher-temperature maxima and shoulders in the $0.6 \leq x \leq 0.8$ susceptibility curves, which have been interpreted as the charge- and orbital-ordering temperatures (see text). The temperature of the negative inflection point of the logarithmic resistivity curve, T_I at $x=0.7$ (square in the figure), is coincident with T_{CO} , further supporting the charge-ordering assignment at this composition. T_N is the inflection point in the magnetic susceptibility for $0.6 \leq x \leq 0.8$ and has been associated with the onset of long-range AF order. T_F denotes the temperature of the onset of a FM moment at the canted-AF ordering in the $0.85 \leq x \leq 1.0$ range. The temperature range above the long-range magnetic ordering temperature where evidence has been found for short-range antiferromagnetic fluctuations (AFF's) is indicated by dotted-shading. T_F^* is analogous with T_F for the $x=0.825$ sample, but is differentiated due to its anomalously high temperature. Finally, note the temperatures T_P , which identify the ZFC, low-temperature maxima in the susceptibility in the $x > 0.8$ range.

correlations (or FMF's) are relatively strong at this composition. In the $\text{La}_{1-x}\text{Ca}_x\text{MnO}_3$ materials, the pronounced increase in $\rho(T)$ and decrease in $\chi(T)$, upon CO, ordering have been ascribed to localization of the holes and the concomitant suppression of the high-temperature FMF.^{26,27} It was with this in mind that the label of T_{CO} was chosen for the χ vs T maximum in Fig. 8(b).

Noting that the θ parameters at $x=0.6$ and 0.8 are larger, we conclude that the FM correlations at these concentrations are weaker than in the $x=0.7$ material (see Fig. 9, top). These materials manifest subtle shoulders in $\chi(T)$ near 280 K, precisely where the intervening phase ($x=0.7$) $\chi(T)$ showed a pronounced peak [see Figs. 8(a) and 8(c)]. We propose that these shoulder features also mark the onset of a CO ordering state similar to (albeit less robust) than that in the $x=0.7$ material. Accordingly these shoulders have been labeled as T_{CO} in Figs. 8(a) and 8(c). As emphasized in the preceding paragraph, the sharp maximum in $\chi(T)$ in CO manganates is attributed to the quenching of FM correlations. The more subtle $\chi(T)$ shoulders of our $x=0.6$ and 0.8 materials are therefore consistent with their weaker FM correlations. The absence of a distinctive resistivity anomaly in these materials could also be related to their weakened FM correlations.

A second (perhaps related) cause for a robust charge ordering in the $x=0.7$ material, but a more tenuous order in the $x=0.6$ and 0.8 materials, could be the closeness of the former to $x=2/3$. In the 3D perovskite manganates (e.g., $\text{La}_{1/3}\text{Ca}_{2/3}\text{MnO}_3$ (Ref. 26 and 28) and $\text{Bi}_{1-x}\text{Ca}_x\text{MnO}_3$ (Ref. 28)) the CO ordering effects are most pronounced for hole concentration near certain fractional values.^{26,28} At such concentrations the ordering is the simplest and most robust. Moreover, the precise-fractional-concentration effects are much more dramatic for CO ordering in the 2D $\text{La}_{1-x}\text{Sr}_x\text{NiO}_4$ system.^{25,29} Indeed, away from such fractional compositions in the nickelate series, severely reduced magnetic and resistivity anomalies are seen and electron diffraction evidences weaker CO correlations.^{25,29} Thus a peaking of the 3D correlations in the CO ordering (and their magnetic and transport signatures) near $x=2/3$ (i.e., the $x=0.7$ material) in our reduced dimensional system appears to be reasonable.

Single-crystal or oriented thin film studies of the a - b plane vs c axis resistivity would be very useful in addressing the issues raised above. Further experiments, such as variable-temperature electron or neutron diffraction, would be particularly important to pin down both the CO ordering proposed and the degree of the interlayer correlations.

We will now turn to the 100–150 K temperature region where magnetic-ordering correlations show an onset change in all of the materials. In close proximity to the ordering temperature T_N , in a 3D material one typically observes a sharp peak in $\chi(T)$ with a peak in $d\chi/dT$ just below it. In a quasi-2D AF material, T_N is identified with a much broader inflection point in $\chi(T)$ (peak in $d\chi/dT$). In such quasi-2D materials the antiferromagnetic fluctuations (AFF's) weaken slowly above T_N , leading to a broad maximum in $\chi(T)$ well above T_N . In the inverse susceptibility [$\chi^{-1}(T)$], these AFFs are reflected by an upturn from CW behavior. With these points in mind, the evidence for low-temperature AF interactions in our materials will be discussed.

In the $x=0.6$, 0.7 , and 0.8 materials [see Figs. 8(a)–8(c)] it can be seen that they all exhibit a positive inflection in the $\chi(T)$ curves at temperatures in the 100–150 K range (labeled T_N in the figures). The $x=0.6$ and 0.8 $\chi(T)$ results show maxima at temperatures roughly 50 K above the inflection temperature. As noted, such behavior is typical of 2D AF order, where the inflection point at T_N is associated with

the onset of long-range AF order and the temperature range between T_N and the $\chi(T)$ maximum is associated with the 2D AFFs. Here the AF order occurs within the already charge- and orbital-ordered phase. The region of AFF's above T_N is indicated by a dotted-shaded region in the $\chi(T)$ and $\chi^{-1}(T)$ curves in Figs. 8(a)–8(b).

In the $x=0.7$ material the AFF peak is reduced to a shoulder on the low-temperature side of the robust CO ordering peak at T_{CO} [Fig. 8(b)]. Magnetic and neutron studies have definitively demonstrated that this same behavior is associated with the AF ordering occurring below the CO ordering in the $\text{Bi}_{1-x}\text{Ca}_x\text{MnO}_3$ and $\text{La}_{1-x}\text{Ca}_x\text{MnO}_3$ system.^{26–28}

For $x \geq 0.85$, the susceptibility curves show a dramatic change in behavior [see Figs. 8(e)–8(h)] with the onset of magnetic order (still near 115 K), being accompanied by the development of a modest FM component. This modest net moment is presumably related to canted-AF (CAF) ordering and the ordering temperatures are hereafter designated as T_F (to underscore the FM component). For the $x=0.85$, 0.875, and 1.00 materials, there is a subtle anomalous maximum in the $\chi(T)$, occurring at ~ 50 K above T_F . We attribute this maximum to 2D AFF's, similar to those observed in the $x \leq 0.8$ range. In this composition range, the $\chi(T)^{-1}$ curves in the insets also reflect these AFF's as an extended range of deviation from the high-temperature CW behavior. Again, the AFF temperature region is indicated by a dotted-shaded bar.

For the $x=0.9$ material no local maximum in $\chi(T)$ is present; however, a subtle deviation from CW behavior in the $\chi(T)^{-1}$ indicates AFF's consistent with that of the neighboring compositions. While encountering a somewhat disparate magnetic behavior in this $x=0.9$ material, it should be noted that in such quasi-2D systems competing magnetic interactions can lead to modestly different behavior at isolated compositions. Despite a small detailed deviation, the $x=0.9$ magnetic behavior appears to basically fit in with the results of the other materials in the $x \geq 0.85$ composition range.

Thus in the $0.85 \leq x \leq 1.0$ range the susceptibility results indicate a canted-AF-ordered state with a small FM moment (through the canting) below T_F with 2D AFF effects apparent in the temperature range above T_F . In this composition range the low-temperature ZFC susceptibility also exhibits maximum (at a temperature T_P) which disappears in the FC susceptibility. This low-field maximum could reflect disorder and frustration effects or domain effects.

The magnetic results thus far clearly reflect the presence of a boundary between the CAF order and CO-plus-AF order in the $0.8 < x < 0.85$ range (Fig. 9). However, the magnetic behavior of the $x=0.825$ material is not simply straddling this crossover. The susceptibility curve for the $x=0.825$ material manifests a truly singular behavior [see Fig. 8(d)] relative to the other materials in this entire series. While it does develop a small, low-temperature FM moment near 115 K (as the $x \geq 0.85$ materials), it also first develops a spontaneous moment at a higher temperature $T_F^* \cong 280$ K. Close inspection of the $\chi(T)^{-1}$ curve [Fig. 8(d) inset] also reveals a departure from the high- T CW behavior in the 50 K range above T_F^* . This behavior is reminiscent of that in the $0.85 \leq x \leq 1.0$ range; however, it occurs at an unprecedentedly

high temperature (more comparable to that of the proposed charge-ordering energy in the $x \geq 0.6$ regime). The magnetic behavior of the $x=0.825$ material was sufficiently singular that it was prepared a second time by another member of our group. The independent preparation produced identical results. It is worth noting that the θ value of the $x=0.825$ material is the lowest of the entire series consistent with anomalously strong FM correlations and the singularly high T_F^* at this composition. Speculation on this behavior would be premature at this juncture.

F. Magnetic phase diagram summary

Figure 9 is intended as a guide to help summarize the rather complicated magnetic results of the $\text{La}_{2-2x}\text{Ca}_{1+2x}\text{Mn}_2\text{O}_7$ ($0.6 \leq x \leq 1.0$) system. Figure 9 compares the composition dependence of the high- T Weiss parameters (top), low- T susceptibility and high- T resistivity (middle), and the locality of the magnetic-transport-feature-related temperatures in a proposed phase diagram (bottom). The most basic feature of the $\text{La}_{2-2x}\text{Ca}_{1+2x}\text{Mn}_2\text{O}_7$ system appears to be a crossover between two regimes of behavior in the $x \leq 0.8$ and $x \geq 0.85$ ranges, respectively.

In the $x \leq 0.8$ range we have proposed that at high temperatures ferromagnetic fluctuations (FMF's), although masked by covalency effects, are present; a charge- and orbital-ordering transition occurs at a temperature $T_{CO} \cong 280$ K; at lower temperatures, 2D AFF's arise at 170–200 K as indicated by a dotted-shaded range in the phase diagram (Fig. 9, bottom); these correlations are followed by the onset of long-range AF ordering at T_N in the 110–140 K range. The robustness of the CO signature appears to vary with strength of the high- T FMF's and/or with the nearness of the composition to a commensurate $\text{Mn}^{3+}/\text{Mn}^{4+}$ ratio. Specifically, our $x=0.7$ material exhibits the clearest charge- and orbital-ordering anomalies with the $x=0.6$ and 0.8 materials manifesting more subtle apparently shorter-range charge- and orbital-ordering signatures.

In the $x \geq 0.85$ range the low-temperature state appears to be that of a CAF with a small FM moment below a long-range ordering temperature $T_F \cong 115$ K. There is some evidence for 2D AFFs in the 160–180 K range (as indicated by dotted shading in the phase diagram). The rapid rise in the susceptibility at 10 K (in Fig. 9, middle) reflects the low-temperature crossover from CO-AF order for $x \leq 0.8$ to CAF order for $x > 0.8$. Interestingly, a similar crossover from CO-AF order to CAF order occurs in essentially the same composition range for the 3D perovskite $\text{Bi}_{1-x}\text{Ca}_x\text{MnO}_3$ system.²⁹ The resistivity at 300 K (Fig. 9, middle) also manifests structure marking the crossover near $x=0.8$; however, the presence of the insulating (La,Ca)O layers between the perovskite (La,Ca)MnO₃ layers complicates its interpretation. Recall also that the a and c lattice parameters (Fig. 3) exhibited nonlinear changes across the $x=0.8$ phase diagram transition region.

The singular behavior at $x=0.825$ must be noted in this summary and in the phase diagram. The magnetic phase transition, at T_F^* , with a FM component, is clearly anomalous. The possibility that the susceptibility shoulder at 270 K in the $x=0.8$ material is in fact associated with an AF transition (as opposed to the CO ordering assigned by us) must

be considered. This would at least provide precedence for such a high magnetic interaction energy scale at $x=0.825$. In this scenario the lower transition at $x=0.8$ would reasonably be associated with the rapidly dropping charge and orbital ordering. Low-temperature electron diffraction and magnetic experiments in the $0.8 \leq x \leq 0.85$ transition region are currently being planned to clarify these issues.

The loci of the low-temperature, ZFC maxima (T_p) have been indicated in the phase diagram. This low-field, low-energy scale may reflect magnetic disorder and frustration effects or domain behavior and is included for completeness. It is not unreasonable, however, that the FM-AF frustration effects would become more important close to the CAF-to-CO-plus-AF boundary in the $0.8 \leq x \leq 0.85$ compositions. Finally, the possibility of additional structure in the phase diagram below T_F should be noted. Certainly, the susceptibility versus temperature curves do show breaks in their slope and an anomalous quasilinear thermal variation. In a system with varying AF and FM interactions, with the added charge- and orbital-ordering degree of freedom and low-dimensionality effects, the possibility of competing orderings and/or commensurability changes must be considered.

IV. CONCLUSION

In conclusion, the $\text{La}_{2-2x}\text{Ca}_{1+2x}\text{Mn}_2\text{O}_7$ ($0.6 \leq x \leq 1.0$) series has been successfully prepared and the structural, magnetic, and transport properties of Mn^{4+} -rich layered RP manganates were investigated. Mn K XAS results indicate that the average Mn valence in this layered system is not at strong variance with the 3D perovskite analog (with the $x=0.6$ material being a possible exception). The structural and magnetic properties evidence a crossover in the physical properties near the $x=0.8$ composition. Below $x=0.8$ the materials appear to involve separate charge-orbital- and AF-ordering transitions. For $x>0.8$ canted-AF order (with a FM component) arises. Finally, the need for additional work in the $0.8 \leq x \leq 0.85$ range to clarify the charge-orbital and magnetic transitions is noted.

ACKNOWLEDGMENT

This work was supported by NSF–Solid State Chemistry Grant No. DMR 96-13106.

-
- ¹C. N. R. Rao, A. K. Cheetham, and R. Mahesh, *Chem. Mater.* **8**, 2421 (1996), and references therein.
- ²C. N. R. Rao, A. Arulraj, P. N. Santosh, and A. K. Cheetham, *Chem. Mater.* **10**, 2174 (1998), and references therein.
- ³C. Zener, *Phys. Rev.* **82**, 403 (1951).
- ⁴P. Schiffer, A. P. Ramirez, W. Bao, and S.-W. Cheong, *Phys. Rev. Lett.* **75**, 3336 (1995).
- ⁵Y. Tokura, Y. Tomioka, H. Kuwahara, A. Asamitsu, Y. Moritomo, and M. Kasai, *J. Appl. Phys.* **79**, 5288 (1996).
- ⁶S. N. Ruddlesden and P. Popper, *Acta Crystallogr.* **11**, 541 (1958).
- ⁷P. D. Battle and M. J. Rosseinsky, *Curr. Opin. Solid State Mater. Sci.* **4**, 163 (1999), and references therein.
- ⁸Y. Moritomo, A. Asamitsu, H. Kuwahara, and Y. Tokura, *Nature (London)* **380**, 141 (1996).
- ⁹P. D. Battle, S. J. Bludell, M. A. Green, W. Hayes, M. Honold, A. K. Klehe, N. S. Laskey, J. E. Millburn, L. Murphy, M. J. Rosseinsky, N. A. Samarin, J. Singleton, N. E. Sluchanko, S. P. Sullivan, and J. F. Vente, *J. Phys.: Condens. Matter* **8**, L427 (1996).
- ¹⁰H. Asano, J. Hayakana, and M. Matsui, *Phys. Rev. B* **56**, 5345 (1997).
- ¹¹H. Asano, J. Hayakana, and M. Matsui, *Appl. Phys. Lett.* **68**, 3638 (1996).
- ¹²F. Licci, G. Turilli, and P. Ferro, *J. Magn. Magn. Mater.* **164**, L268 (1996).
- ¹³C. Larson and R. B. von Dreele (unpublished).
- ¹⁴P. D. Battle, D. E. Cox, M. A. Green, J. E. Millburn, L. E. Spring, P. G. Radaelli, M. J. Rosseinsky, and J. F. Vente, *Chem. Mater.* **9**, 1042 (1997).
- ¹⁵P. D. Battle, J. A. Hepburn, J. E. Millburn, P. G. Radaelli, M. J. Rosseinsky, L. E. Spring, and J. F. Vente, *Chem. Mater.* **9**, 3215 (1997).
- ¹⁶J. E. Millburn, J. F. Mitchell, and D. N. Argyriou, *Chem. Commun. (Cambridge)* **1999**, 1389.
- ¹⁷S. E. Dann, M. T. Weller, and D. B. Currie, *J. Solid State Chem.* **97**, 179 (1992).
- ¹⁸R. Seshadri, C. Martin, A. Maignan, M. Hervieu, B. Raveau, and C. N. R. Rao, *J. Mater. Chem.* **6**, 1585 (1996).
- ¹⁹D. Fawcett, J. E. Sunstrom, M. Greenblatt, M. Croft, and K. V. Ramanujachary, *Chem. Mater.* **10**, 3643 (1998).
- ²⁰M. Croft, D. Sills, M. Greenblatt, C. Lee, S.-W. Cheong, K. V. Ramanujachary, and D. Tran, *Phys. Rev. B* **55**, 8726 (1997).
- ²¹H. Asano, J. Hayakawa, and M. Matsui, *Phys. Rev. B* **56**, 5395 (1997).
- ²²Z. Zeng, M. Greenblatt, and M. Croft, *Phys. Rev. B* **59**, 8784 (1999).
- ²³S. Elfimov, V. I. Anisimov, and G. A. Sawatzky, *Phys. Rev. Lett.* **82**, 4264 (1999).
- ²⁴H. Chiba, M. Kikuchi, K. Kusaba, Y. Muraoka, and Y. Syono, *Solid State Commun.* **99**, 499 (1996).
- ²⁵H. Woo, T. Tyson, M. Croft, S.-W. Cheong, J. Woicik, and B. Brandt (unpublished).
- ²⁶M. T. Fernández-Díaz, J. L. Martínez, J. M. Alonso, and E. Herrero, *Phys. Rev. B* **59**, 1277 (1999).
- ²⁷Y. Murakami, D. Shindo, H. Chiba, M. Kikuchi, and Y. Syono, *Phys. Rev. B* **55**, 15 043 (1997).
- ²⁸See S.-W. Cheong and C. H. Chen, in *Colossal Magnetoresistance and Related Properties*, edited by C. N. R. Rao and B. Raveau (World Scientific, Englewood Cliffs, NJ, 1999), p. 241 (and references therein).
- ²⁹C. H. Chen, S.-W. Cheong, and A. S. Cooper, *Phys. Rev. Lett.* **71**, 2461 (1994); S.-W. Cheong, H. Hwang, C. H. Chen, B. Battlog, L. Rupp, and S. Carter, *Phys. Rev. B* **49**, 7088 (1994).